

Non-Hermitian zero-mode laser in a nanophotonic trimer

Kaiwen Ji, Bruno Garbin, Melissa Hedir, Juan A. Levenson, and Alejandro Yacomotti ^{*}
*Centre de Nanosciences et de Nanotechnologies, CNRS, Université Paris-Sud, Université Paris-Saclay,
 10 Boulevard Thomas Gobert, 91120 Palaiseau, France*



(Received 7 February 2023; accepted 24 May 2023; published 8 June 2023)

Non-Hermitian zero modes in arrays of coupled optical elements can be tailored to feature a number of interesting properties. In addition to being immune to coupling disorders and remaining pinned at the center of the spectrum, they are not dark modes in general (light intensity does not necessarily vanish in one sublattice), their energy eigenvalues are not restricted to the center of the complex plane, and they can be brought to laser oscillation by carefully patterning the spatial pump profile. In this work, we report on the direct observation of a lasing zero mode in a non-Hermitian three-coupled nanocavity array. We show efficient excitation for nearly equal pump power in the two extreme cavities. Furthermore, its efficiency can be dynamically controlled by pumping the center cavity. The realization of zero-mode lasing in large arrays of coupled nanolasers has potential applications in laser-mode engineering and it opens up promising avenues in optical computing.

DOI: [10.1103/PhysRevA.107.L061502](https://doi.org/10.1103/PhysRevA.107.L061502)

Majorana zero modes are collective excitations pinned at the middle of a gapped band structure. Their topological and non-Abelian properties make them immune against certain types of disorder, and therefore robust for applications in topological quantum computing [1]. While Majorana zero modes usually refer to bound state quasiparticles in superconducting systems, robust zero modes can also be found in photonic devices, having been experimentally demonstrated in a few different platforms, such as flat band structures in optical waveguide arrays [2,3] and topologically protected gap modes in a one-dimensional Su-Schrieffer-Heeger (SSH) chain [4–6]. The zero modes originate, in these experiments, from the chiral—or sublattice—symmetry, $\{H, C\} = 0$, where H is the Hamiltonian and C a unitary operator. On the other hand, the zero modes that have been observed in condensed matter physics and topological superconductors [7–9] result from particle-hole symmetry (PH, also known as charge-conjugation symmetry), where the Hamiltonian anticommutes with an antiunitary operator CT ($\{H, CT\} = 0$, where T is the time reversal operator).

In the Hermitian limit, both chiral and particle-hole symmetries ensure that the eigenvalues always appear in pairs, $\epsilon_i = -\epsilon_j$ [10]. Such a symmetrical band leads to a zero mode with $\epsilon = 0$ for $i = j$. However, in the non-Hermitian (NH) realm, the eigenvalues are generally complex and the imaginary parts account for loss/gain rates. Consequently, the chiral and particle-hole symmetries generally result in different eigenvalue spectra, i.e., $\epsilon_i = -\epsilon_j$ still holds for the chiral symmetry case [11], while $\epsilon_i = -\epsilon_j^*$ takes place in systems with non-Hermitian particle-hole (NHPH) symmetry [12], where the $*$ is the complex conjugate. Therefore, the zero mode features $\text{Re}[\epsilon] = 0$ for the NHPH symmetry, meaning that the non-Hermitian zero mode is more robust than its Hermitian counterpart, since no restriction is applied

to its imaginary part. Recently, NHPH-symmetry protected zero mode has been demonstrated in photonic systems such as a PT -symmetric waveguide array with defect and topological segment [13,14]. However, in those approaches, only one zero mode can be realized at a given spatial location, for instance, the defect or the topological boundary. On the other hand, zero modes warranted by NHPH symmetry in a three-coupled photonic crystal cavity array have been reported recently [15]; there, the zero modes were revealed through photoluminescence experiments and were found to be mainly localized in one sublattice. However, single-spot pumping conditions prevented efficient excitation and therefore no lasing zero mode could be observed. In Ref. [16], spatial modulation of the optical pump in a photonic microring molecule using a knife edge has enabled laser operation at the zero mode through PT -symmetry breaking for sensing applications. Let us stress an important feature of realizing a NHPH-symmetry protected zero-mode laser in cavity arrays: the laser frequency is pinned at the center of the spectrum, and it is insensitive to coupling perturbations.

In this work, we report on the direct observation of a lasing zero mode in a three-coupled nanocavity array with embedded quantum wells (QWs). The lasing condition is enabled by spatially patterning the pump spot by means of a spatial light modulator (SLM). In our three-cavity case, at least one zero mode is expected to exist at the frequency of the single cavity because the number of cavities is odd [10], and it can be efficiently excited above the laser threshold by pumping the two extreme cavities with similar optical powers. Furthermore, we dynamically control the emission intensity by varying the pump power in the center cavity. Ultimately, this building block could be extended to a two-dimensional (2D) network supporting an arbitrary number of zero modes warranted by NHPH symmetry with different intensity distributions [10].

We first consider a three-coupled photonic crystal (PhC) nanocavity array [see Fig. 1(a)] that supports a zero mode. The two extreme cavities (sublattice A) are evanescently coupled

^{*}alejandro.gacomotti@c2n.upsaclay.fr

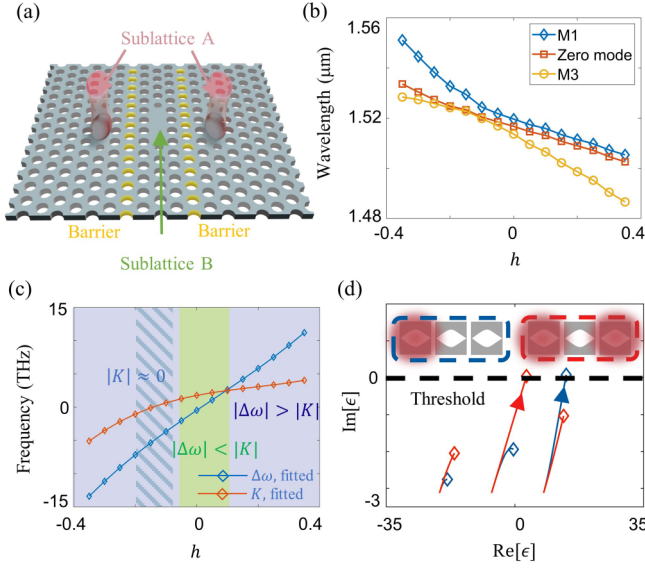


FIG. 1. (a) Schematic of the three-coupled cavity system. The yellow arrays represent the barriers. (b) FDTD simulations showing the mode structure as a function of barrier size h . (c) Coupling and cavity detuning extracted from the hybrid mode frequency splitting and average of two-coupled PhC cavities' 3D FDTD numerical simulation. Solid lines are third-order polynomial fittings, which are subsequently used for CMT calculation with three-coupled cavities in the main text. (d) Evolution of eigenvalues; the arrows indicate the direction of trajectories, and the black dashed line represents the laser threshold $\text{Im}[\epsilon] = 0$. Here, P increase from 0 to P_0 and $1.45P_0$ (where P_0 is the threshold of a single cavity) for pumping two extreme cavities (red curves) and pumping a single cavity (blue curves), respectively. The diamonds represent the end point. Here the parameters are $\tau = 7.1$ ps, $\beta = 0.017$, $\alpha = 3$, $\gamma_{\parallel} = 2.2$ GHz, $\gamma_{\text{tot}} = 5$ GHz, $K = 10/\tau$, $n_0 = 10^{18} \text{ cm}^{-3} \times V_a$, with $V_a = 0.016 \times 10^{-12} \text{ cm}^3$ being the volume of active material.

to the central one (sublattice B). The coupling K can be controlled using the so-called barrier engineering technique [15,17], namely, the radius of the barrier holes [yellow holes in Fig. 1(a)] is modified as $r_b = r_0(1+h)$, where $r_0 = 0.266a$ is the radius of the ordinary air holes and a is the lattice constant. Note that such barrier modulation also introduces additional frequency detunings $\Delta\omega_j$. Given the fact that the central cavity is surrounded by two barriers, we can assume that the detuning in the center is twice the one in the two extreme cavities, $\Delta\omega_{1,3} = \Delta\omega$, $\Delta\omega_2 = 2\Delta\omega$, the sublattice detuning being $\Delta\omega_2 - \Delta\omega_{1,3} = \Delta\omega$. Three-dimensional (3D) finite-difference time-domain (FDTD) simulations, as displayed in Fig. 1(b), are performed to reveal the mode structure of the optical trimer as a function of the barrier size. To further study the impact of the barrier perturbation h on the coupling K and the sublattice detuning $\Delta\omega$, we carried out another simulation using two-coupled PhC cavities and fitted the mode-frequencies with linear coupled mode theory (CMT) [see Fig. 1(c)]. The results can be divided into two different regions: weak cavity coupling, where $|\Delta\omega(h)| > |K(h)|$ (purple), and strong cavity coupling, where $|\Delta\omega(h)| < |K(h)|$ (green background). A particularly interesting domain (dashed background) is $-20\% \leq h \leq -10\%$, where the coupling approaches zero ($|K| \approx 0$). In this region, the center

cavity is effectively decoupled from the other two and the zero mode becomes one of the eigenmodes of an effective dimer formed by sublattice A; such a parameter regime will be used later on to relate the zero-mode frequency to the single-cavity one.

We model our system using carrier-dependent coupled mode theory (CD-CMT) [15,18] that governs the time evolution of coupled complex field amplitudes $a = [a_1, a_2, a_3]^T$ in the semiconductor cavities, in the presence of carrier populations n_j , $j = 1, 2, 3$:

$$\frac{da}{dt} = iHa + F(t), \quad (1)$$

$$H = \begin{pmatrix} \omega_0 + \alpha g_1 + \Delta\omega_1 & K & 0 \\ K & \omega_0 + \alpha g_2 + \Delta\omega_2 & K \\ 0 & K & \omega_0 + \alpha g_3 + \Delta\omega_3 \end{pmatrix} - i \begin{pmatrix} g_1 - \frac{1}{\tau} & 0 & 0 \\ 0 & g_2 - \frac{1}{\tau} & 0 \\ 0 & 0 & g_3 - \frac{1}{\tau} \end{pmatrix}, \quad (2)$$

$$\frac{dn_j}{dt} = P_j - n_j\gamma_{\text{tot}} - \beta\gamma_{\parallel}(n_j - n_0)|a_j|^2, \quad (3)$$

where ω_0 and τ are the resonant frequency and cavity-damping time of a single transparent cavity, respectively, $g_j = \beta\gamma_{\parallel}(n_j - n_0)/2$ are the gain rates, β is the spontaneous emission factor, γ_{\parallel} is the two-level radiative recombination rate, α is linewidth enhancement—or Henry—factor, n_0 represents the carrier number at transparency, P_j are the pump rates, and γ_{tot} is the total carrier recombination rate. $F(t) = [F_1(t), F_2(t), F_3(t)]^T$ represent Langevin noise terms accounting for spontaneous emission. Here, $\langle F_{\mu}(t)F_{\nu}^*(t') \rangle = 2D_{\mu\nu}\delta(t-t')$ and $\langle F_{\mu}(t)F_{\nu}(t') \rangle = 0$. The coefficient is $D_{\mu\nu} = R_{sp}\delta_{\mu\nu}/2$, with R_{sp} being the spontaneous emission rate $R_{sp} = \beta F_p B n_{1,2}^2/V_a$, where F_p is the Purcell factor, B is the bimolecular radiative recombination rate, and V_a is the volume of the active medium (parameter values are given in the captions of Figs. 1 and 3; more details can be found in Ref. [18]).

We start with a simple case where $\Delta\omega_j = 0$, $F_j(t) = 0$ and carrier-induced refractive index change effect is neglected ($\alpha = 0$). When the two extreme cavities are equally pumped we set $g_1 = g_3 = g$ and $g_2 = 0$. Below the laser threshold ($|a_1|^2 = |a_2|^2 = |a_3|^2 \rightarrow 0$), the eigenvalues read

$$\epsilon_0 = \omega_0 - i\left(g - \frac{1}{\tau}\right), \quad (4)$$

$$\epsilon_{\pm} = i\left(\frac{1}{\tau} - \frac{g}{2}\right) \pm \frac{1}{2}\sqrt{8K^2 - g^2} + \omega_0, \quad (5)$$

where ϵ_0 is the NH zero mode with eigenvector being $(1, 0, -1)^T$. Hence, the zero mode is a dark one, i.e., the intensity in one of the sublattices (here sublattice B—the central cavity) vanishes; as a result, a necessary condition to excite it is to pump sublattice A, while pumping sublattice B alone would be inefficient. Noticeably, there is a π -phase difference between the two extreme cavities, due to frustration. This π -phase difference proves to be robust against

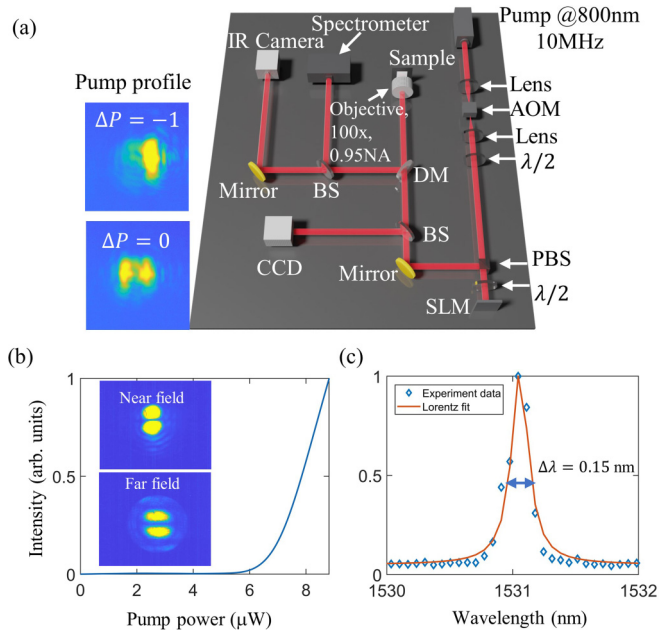


FIG. 2. Experimental characterizations of zero-mode laser. (a) Experiment setup with the SLM; (b) Light-in/light-out curve of the zero-mode laser. The inserts are the near and far fields of the zero-mode laser; (c) Experimental measurement and the Lorentz fit of zero-mode laser.

pump unbalancing, and it is a useful fingerprint to identify it experimentally [15].

Figure 1(d) shows the real and imaginary parts of the eigenvalues of the full—i.e., including α -induced blue-shift effects—Hamiltonian in Eq. (2). When a single extreme cavity is pumped (blue curves), the highest-frequency mode is more efficiently excited and reaches the laser threshold [$\text{Im}(\epsilon) = 0$] first. This can be explained by the spectral overlap between the excited cavity photons and the hybrid modes; namely, the carrier-induced blue-shift of the excited cavity resonance better overlaps with the blue-detuned hybrid mode [15]. In contrast, the zero mode reaches the threshold before the two others and becomes the lasing mode as long as the two extreme cavities are pumped equally (see red curves).

In order to observe the zero-mode laser experimentally, we fabricated the three-coupled PhC cavities in an indium phosphide (InP) suspended membrane, with four embedded $\text{InGa}_{0.17}\text{As}_{0.76}\text{P}$ QWs [19]. We performed photoluminescence (PL) experiments to study the emission properties of the zero mode. We choose a pulsed pump laser (100 ps duration and 10 MHz repetition rate) as the pump source in order to reduce thermal effects. As we discussed before, the zero mode cannot be efficiently excited using only one spot, hence we employ a SLM to reshape the pump configuration. Our liquid-crystal-based SLM is operated in amplitude modulation mode [Fig. 2(a)]. This configuration requires two half-wave plates; the first one (close to the acousto-optic modulator, AOM) is used to maximize the transmission through the PBS, and the second one (close to the SLM), whose optic axis is rotated 22.5° with respect to the horizontal plane, maximizes the contrast between the pump pattern and the background. Such a modulation allows us to control the pump intensities

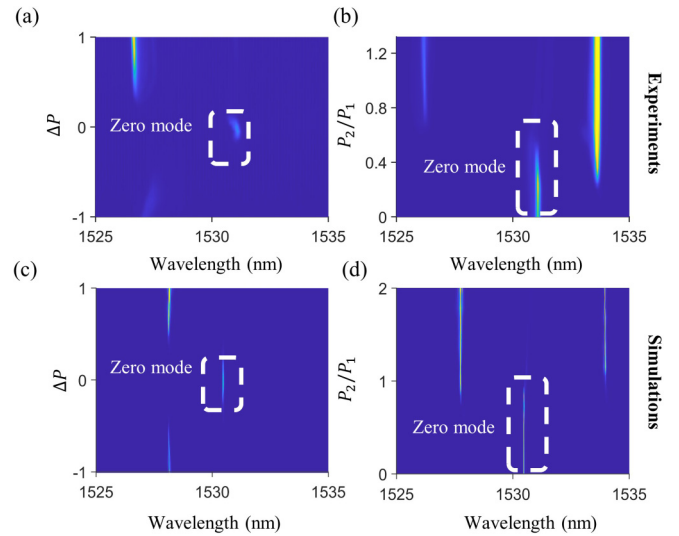


FIG. 3. Experimental observation of zero-mode laser in the strong coupling region ($h = 0\%$ and lattice constant is $a = 408$ nm). (a) PL map when the pumps in the two extreme cavities are unbalanced; (b) PL map when the pump in the center cavity is increased. Dashed boxes indicate location of zero-mode laser. (c) and (d) are the simulations of (a) and (b), respectively. Here in the simulations we use $K = 12.5/\tau$, $\Delta\omega_1 = \Delta\omega_3 = -3.38/\tau$, $\Delta\omega_2 = 2\Delta\omega_{1,3}$, $\omega_0 = 195.81$ THz, $P_1 + P_2 = 3P_0$, with P_0 being the threshold for the single cavity. For Langevin noise terms, the Purcell factor and the bimolecular radiative recombination rate are taken as $F_p = 1.03$ and $B = 3 \times 10^{10} \text{ cm}^3 \text{ s}^{-1}$, respectively.

in three cavities independently. Two typical pump patterns are depicted in the insets of Fig. 2(a). The modified pump laser is then focused down on the sample through a microscope objective (100 \times IR with 0.95 NA) and the radiated PL is spectrally resolved with a spectrometer.

We characterize the nanolaser emission under nearly equal pumping of the two extreme cavities. The light-in/light-out emission [Fig. 2(b)] together with the emission linewidth [Fig. 2(c)] are strong evidences of a zero-mode laser obtained in the strong intercavity coupling region ($h = 0\%$, for which $|K| \gg |\Delta\omega|$), at $\lambda \approx 1531.11$ nm. In Fig. 2(b) a clear laser threshold is observed for an average pump power of about 6 μW . To verify that such a mode is indeed a zero mode, we measure its near- and far-field patterns using an InGaAs infrared camera. In the near field, no energy is detected in the center; in addition, the far-field image shows vanishing intensity in the center, revealing an antisymmetric field distribution [20] [insets in Fig. 2(b)]. As discussed before, a π phase difference between the two extreme cavities is compatible with the frustration mechanism at the origin of the zero mode.

With the aim of further testing the robustness of the zero-mode laser, we define a control parameter $\Delta P = (P_3 - P_1)/(P_1 + P_3)$ that conserves the total pump power ($P_1 + P_3 = \text{const}$). Panel (a) in Fig. 3 shows the spectral intensity as a function of both wavelength and ΔP . Note that only one of the extreme cavities is pumped when $\Delta P = \pm 1$, and both of them are pumped equally when $\Delta P = 0$. The zero-mode laser is efficiently excited in the range $|\Delta P| \leq 0.15$. Figure 3(c) depicts the numerical calculation results using Eqs. (1)–(3), showing very good agreement with the experiment.

Interestingly, we can control the zero-mode laser by injecting power in the center cavity ($P_1 = P_3, P_2 = 0 \rightarrow 1.2P_1$); the experimental results are displayed in Fig. 3(b). Figure 3(d) shows the corresponding simulation results, which are in good agreement with the experiment. We observe that the zero persists as long as the center cavity is absorptive, namely, $g_2 \leq 0$, which takes place for $P_2/P_1 < 0.5$; yet, at the onset of net gain in the center cavity ($g_2 > 0$), the zero mode switches off and the energy is transferred to side modes. This result implies that the visibility of the zero-mode laser can be dynamically controlled by varying the pump power in the center cavity.

A most important property of a lasing zero mode is that its frequency should correspond to the single-cavity one, in this case modified by the presence of a barrier, $\omega_0 + \Delta\omega$. However, it is difficult to directly compare the zero mode with the single cavity nanolaser experimentally because the latter would belong to a different lithographic realization, therefore it is likely to be detuned with respect to the coupled cavity central frequency. In order to cope with this, we move to a weaker coupling regime in which we can effectively decouple the system by unbalancing the optical pumping.

As predicted in Fig. 1(c), the coupling is near zero in the range of $-20\% \leq h \leq -10\%$, the center cavity (sublattice B) becomes decoupled from sublattice A, and therefore the system can be treated as an effective optical dimer given by the two-coupled extreme cavities [15]. In order to compute the effective coupling parameters we apply the Schrieffer-Wolff transformation [21,22] to the Hamiltonian in Eq. (2) (here, for the sake of simplicity, we take $\alpha = 0$ and only consider Hermitian terms). As long as $K \ll \Delta\omega$, we have

$$H_{\text{eff}} = \hat{U}^\dagger H \hat{U} \approx \begin{pmatrix} \omega_0 + \Delta\omega_{\text{eff}} & K_{\text{eff}} & 0 \\ K_{\text{eff}} & \omega_0 + \Delta\omega_{\text{eff}} & 0 \\ 0 & 0 & \omega_0 + \Delta\omega'_{\text{eff}} \end{pmatrix}, \quad (6)$$

with the eigenvectors being $[a_1, a_3, a_2]^T$. Here \hat{U} is a unitary operation used to decouple the center cavity from the rest of the system. The effective coupling strength reads $K_{\text{eff}} = K^2/\Delta\omega$, and the effective detunings for the extreme and center cavities are $\Delta\omega_{\text{eff}} = K^2/\Delta\omega + \Delta\omega$ and $\Delta\omega'_{\text{eff}} = 2K^2/\Delta\omega + 2\Delta\omega$, respectively. The eigenvalues of the 2×2 block of H_{eff} are

$$\epsilon_- = \Delta\omega + \omega_0, \quad (7)$$

$$\epsilon_+ = \Delta\omega + \frac{2K^2}{\Delta\omega} + \omega_0. \quad (8)$$

Equations (7) and (8) are the hybrid frequencies of the effective dimer. Equation (7) implies that the effective zero mode in the dimer is lasing at the frequency of the uncoupled extreme cavity. Note that, unlike the conventional two-coupled cavities, where the eigenfrequencies are split symmetrically with respect to the uncoupled cavity frequency, here the two eigenvalues of the effective dimer are not equally distant from the single-cavity frequency. Table I displays the parameters of the effective dimer. Clearly, in the range $-20\% \leq h \leq -10\%$, the effective coupling is much smaller (in absolute value) compared to the actual one. Thus, unlike Figs. 3(a) and 3(c), unbalancing the pumping may effectively decouple

TABLE I. Comparison of the couplings and detunings between actual and the effective two-coupled cavities. Parameters are normalized to the single-cavity loss rate $1/\tau$.

h	-20%	-15%	-10%	-5%
K (actual two cavities)	-7.44	-0.84	4.57	8.96
K_{eff}	1.08	0.018	0.80	5.51
$\Delta\omega$ (actual two cavities)	-50.91	-38.16	-26.09	-14.56
$\Delta\omega_{\text{eff}}$	-104.00	-76.35	-53.79	-40.14

the extreme cavities, and therefore the single-cavity frequency can be directly compared with that of the zero mode.

In the following we measure the PL maps in the small coupling region. We point out that the zero mode is only warranted for nonzero coupling, therefore vanishing coupling, predicted for $h = -15\%$ (Fig. 1), must be avoided; we then choose, for this experiment, $h = -20\%$. The results are displayed in Fig. 4(a). As the unbalanced pump parameter ΔP decreases from $\Delta P = 0$ to $\Delta P = -1$, the leftmost mode red shifts and its wavelength approaches that of the zero mode. This observation implies that the zero-mode frequency is close to the one corresponding to a single, uncoupled cavity, albeit perturbed by the presence of the barrier ($\omega_0 + \Delta\omega$). Figure 4(b) shows the simulation results of the effective dimer model, which agrees with the experimental result nicely.

The lasing zero mode demonstrated here is of geometrical nature, i.e., it arises from geometrical frustration. In future realizations, another NH zero mode could be created in similar trimers through, for instance, PT symmetry breaking [16] or the spontaneous restoration of NHPH symmetry [10] at exceptional points.

In conclusion, we have experimentally demonstrated a lasing zero mode in a three-coupled photonic crystal nanocavity array. Such a NH zero mode can be efficiently excited by pumping the two extreme cavities with nearly equal power, surviving within a range of pump power unbalance of 15%. Furthermore, the intensity of the lasing zero mode can be dynamically controlled by pumping the center cavity, which eventually transfers the energy to side modes;

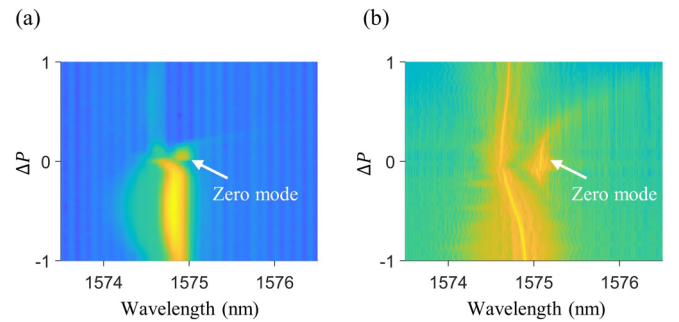


FIG. 4. Observation of zero mode laser in the weak coupling region ($h = -20\%$, $a = 422$ nm). (a) Experimental comparison between the zero-mode laser and the single cavity; the PL map is plotted in logarithmic scale. (b) Simulation result using the effective two-coupled system model. Here the parameters are $K = 1.08/\tau$, $\Delta\omega_1 = 0$, $\Delta\omega_2 = 1.2K$, and $\omega_0 = 190.28$ THz.

noteworthy, we have observed that the zero mode is robust upon increase of the central cavity pump power up to 50% of the extreme cavity pump level. We attribute the observed flexibility in exciting the laser zero mode to the NHPH symmetry protection. This is expected as long as the coupling strength largely overcomes linear and nonlinear detunings, which is verified, in our system, for small barrier perturbations ($h \sim 0$) [15]. We have also shown that the three-coupled cavities can be reduced to an effective dimer when the coupling is weak compared to the sublattice detuning, which is used to actively decouple the system and confirms that the central mode oscillates at a frequency close to that of a single cavity. Our work provides a flexible way to excite and control

the lasing zero mode via SLM pump patterning, whose manipulation and symmetry protection features may be of interest in potential applications such as optical computing [23] and spatial profile tuning of laser arrays [10].

We thank Li Ge for carefully reading our manuscript and providing useful comments. This work is partially supported by French National Research Agency (ANR) Grants No. ANR UNIQ DS078 and No. ANR-22-CE24-0012-01, the European Union in the form of Marie Skłodowska-Curie Action Grant No. MSCA-841351, and by the RENATECH network. K.J. acknowledges the financial support of the China Scholarship Council (No. 202006970015).

-
- [1] C. Nayak, S. H. Simon, A. Stern, M. Freedman, and S. Das Sarma, *Rev. Mod. Phys.* **80**, 1083 (2008).
- [2] R. A. Vicencio, C. Cantillano, L. Morales-Inostroza, B. Real, C. Mejía-Cortés, S. Weimann, A. Szameit, and M. I. Molina, *Phys. Rev. Lett.* **114**, 245503 (2015).
- [3] S. Mukherjee and R. R. Thomson, *Opt. Lett.* **40**, 5443 (2015).
- [4] P. St-Jean, V. Goblot, E. Galopin, A. Lemaître, T. Ozawa, L. Le Gratiet, I. Sagnes, J. Bloch, and A. Amo, *Nat. Photonics* **11**, 651 (2017).
- [5] M. Parto, S. Wittek, H. Hodaei, G. Harari, M. A. Bandres, J. Ren, M. C. Rechtsman, M. Segev, D. N. Christodoulides, and M. Khajavikhan, *Phys. Rev. Lett.* **120**, 113901 (2018).
- [6] C. Han, M. Lee, S. Callard, C. Seassal, and H. Jeon, *Light Sci. Appl.* **8**, 40 (2019).
- [7] H.-H. Sun, K.-W. Zhang, L.-H. Hu, C. Li, G.-Y. Wang, H.-Y. Ma, Z.-A. Xu, C.-L. Gao, D.-D. Guan, Y.-Y. Li *et al.*, *Phys. Rev. Lett.* **116**, 257003 (2016).
- [8] R. M. Lutchyn, E. P. Bakkers, L. P. Kouwenhoven, P. Krogstrup, C. M. Marcus, and Y. Oreg, *Nat. Rev. Mater.* **3**, 52 (2018).
- [9] B. Jäck, Y. Xie, J. Li, S. Jeon, B. A. Bernevig, and A. Yazdani, *Science* **364**, 1255 (2019).
- [10] L. Ge, *Phys. Rev. A* **95**, 023812 (2017).
- [11] J. D. H. Rivero and L. Ge, *Phys. Rev. B* **103**, 014111 (2021).
- [12] D. Pikulin and Y. V. Nazarov, *JETP Lett.* **94**, 693 (2012).
- [13] B. Qi, L. Zhang, and L. Ge, *Phys. Rev. Lett.* **120**, 093901 (2018).
- [14] M. Pan, H. Zhao, P. Miao, S. Longhi, and L. Feng, *Nat. Commun.* **9**, 1308 (2018).
- [15] F. Hentinger, M. Hedir, B. Garbin, M. Marconi, L. Ge, F. Raineri, J. A. Levenson, and A. M. Yacomotti, *Photonics Res.* **10**, 574 (2022).
- [16] H. Hodaei, A. U. Hassan, S. Wittek, H. Garcia-Gracia, R. El-Ganainy, D. N. Christodoulides, and M. Khajavikhan, *Nature (London)* **548**, 187 (2017).
- [17] S. Haddadi, P. Hamel, G. Beaudoin, I. Sagnes, C. Sauvan, P. Lalanne, J. A. Levenson, and A. Yacomotti, *Opt. Express* **22**, 12359 (2014).
- [18] M. Marconi, F. Raineri, A. Levenson, A. M. Yacomotti, J. Javaloyes, S. H. Pan, A. El Amili, and Y. Fainman, *Phys. Rev. Lett.* **124**, 213602 (2020).
- [19] P. Hamel, S. Haddadi, F. Raineri, P. Monnier, G. Beaudoin, I. Sagnes, A. Levenson, and A. M. Yacomotti, *Nat. Photonics* **9**, 311 (2015).
- [20] M. Brunstein, T. J. Karle, I. Sagnes, F. Raineri, J. Bloch, Y. Halioua, G. Beaudoin, L. Le Gratiet, J. A. Levenson, and A. M. Yacomotti, *Appl. Phys. Lett.* **99**, 111101 (2011).
- [21] J. R. Schrieffer and P. A. Wolff, *Phys. Rev.* **149**, 491 (1966).
- [22] Q. Zhong, A. Hashemi, Ş. K. Özdemir, and R. El-Ganainy, *Phys. Rev. Res.* **3**, 013220 (2021).
- [23] G. Tirabassi, K. Ji, C. Masoller, and A. M. Yacomotti, *APL Photonics* **7**, 090801 (2022).